Absolute Calibration of the Infrared Array Camera on the *Spitzer Space Telescope*

William T. Reach,[1] S. T. Megeath,[2] Martin Cohen,[3] J. Hora,[2] Sean Carey,[1] Jason Surace,[1] S. P. Willner,[2] P. Barmby,[2] Gillian Wilson,[1] William Glaccum,[1] Patrick Lowrance,[1] Massimo Marengo,[2] and Giovanni G. Fazio[2]

ABSTRACT. The Infrared Array Camera (IRAC) on the *Spitzer Space Telescope* is absolutely calibrated by comparing photometry of a set of A stars near the north ecliptic pole to predictions based on ground-based observations and a stellar atmosphere model. The brightness of point sources is calibrated to an accuracy of 3%, relative to models for A-star stellar atmospheres, for observations performed and analyzed in the same manner as for the calibration stars. This includes corrections for the location of the star in the array and the location of the centroid within the peak pixel. Long-term stability of the IRAC photometry was measured by monitoring the brightness of A dwarfs and K giants (near the north ecliptic pole) observed several times per month; the photometry is stable to 1.5% (rms) over a year. Intermediate-timescale stability of the IRAC photometry was measured by monitoring at least one secondary calibrator (near the ecliptic plane) every 12 hr while IRAC was in nominal operations; the intermediate-term photometry is stable, with a 1% dispersion (rms). One of the secondary calibrators was found to have significantly time-variable (5%) mid-infrared emission, with a period (7.4 days) matching the optical light curve; it is possibly a Cepheid variable.

1. INTRODUCTION

The Infrared Array Camera (IRAC) was built at NASA Goddard Space Flight Center under the direction of the Smithsonian Astrophysical Observatory (Fazio et al. 2004). It is the mid-infrared camera on the *Spitzer Space Telescope* (Werner et al. 2004), with four arrays observing at 3.6, 4.5, 5.8, and 8 μm. The absolute calibration of the camera was performed in flight by comparing observed to predicted brightness for a set of stars that was selected and characterized before launch (Cohen 2003; Cohen et al. 2003). This paper presents the in-flight calibration results, including the observing strategy, the predictions and measurements, and an assessment of the calibration accuracy and stability of the instrument and the pipeline-processed data provided by the *Spitzer* Science Center (SSC) to observers.

2. CALIBRATOR SELECTION AND OBSERVING STRATEGY

The primary calibrators (Table 1) are a set of A main-sequence and K giant stars. They were chosen from a larger list of candidates on the basis of having good spectral and photometric data and no known evidence of variability (Megeath et al. 2003). The set of plausible calibrators was observed during the in-orbit checkout (IOC) to select which ones would become the primary

calibrators for the nominal mission. Table 2 lists the coordinates of the candidate primary calibrators that were observed during the in-orbit checkout, together with the IRAC channels in which useful data were obtained. Table 1 lists the primary calibrators that have been observed during the nominal mission.

Primary calibrators are observed with all four IRAC arrays during every instrument campaign. The primary calibrators are located in the *Spitzer* continuous viewing zone, a region approximately 10° in radius centered on the north ecliptic pole. The south ecliptic pole is also continuously visible, but it saves observing time to have all calibrators close together on the sky. After the first 6 months of the nominal science mission, the radius of the continuous viewing zone was decreased to 7°.5, making two of the primary calibrators visible for only 8 months each year.

Secondary calibrators are observed approximately every 12 hr while IRAC is on; they are intended to monitor the gain stability during each observing campaign. Because routine *Spitzer* operations require pointing the high-gain antenna at the Earth every ~12 hr to downlink data, we chose a network of secondary calibrators that can be rapidly observed after each downlink. The *Spitzer* orbit is close to the ecliptic plane, and the telescope points opposite the high-gain antenna. Thus, when the antenna points at Earth, the telescope points somewhere near the ecliptic plane at a longitude that changes about once a year. Secondary calibrators spaced along the ecliptic can therefore be observed efficiently before or after telemetry downlinks, with little slewing overhead. The network of secondary calibrators has two stars every 20° of ecliptic longitude. One or two secondary calibrators (Table 3) are chosen for each campaign.

[1] *Spitzer* Science Center, MS 220-6, California Institute of Technology, Pasadena, CA 91125; reach@ipac.caltech.edu.
[2] Harvard-Smithsonian Center for Astrophysics, 60 Garden Street, Cambridge, MA 02138.
[3] Radio Astronomy Laboratory, 601 Campbell Hall, University of California at Berkeley, Berkeley, CA 94720.

TABLE 1
IRAC Primary Absolute Calibrators

Star[a]	Symbol in Fig. 1	Other Name	2MASSJ[b]	Type	A_v	Ks	[3.6]	[4.5]	[5.8]	[8.0]
NPM1p64.0581	■	HD 180609	19124720+6410373	A0 V	0.387	9.117	9.123	9.104	9.107	9.122
HD 165459	▲		18023073+5837381	A1 V	0.285	6.584	6.593	6.575	6.579	6.591
NPM1p60.0581	♦	BD +60°1753	17245227+6025508	A1 V	0	9.645	9.666	9.653	9.659	9.669
1812095	▼		18120956+6329423	A3 V	0.378	11.596	11.275	11.254	11.255	11.265
KF08T3	□		17551622+6610116	K0.5 III	0	11.090	10.944	10.986	10.985	10.943
KF09T1	△	GSC 04212-01074	17592304+6602561	K0 III	0	8.114	8.046	8.087	8.086	8.047
KF06T1	◇		17575849+6652293	K1.5 III	0	10.987	10.762	10.906	10.833	10.793
KF06T2	▽		17583798+6646522	K1.5 III	0.189	11.273	11.065	11.193	11.133	11.095
NPM1p66.0578	○	GSC 04229-01455	19253220+6647381	K1 III	0	8.330	8.249	8.347	8.310	8.335
NPM1p67.0536	▷	SAO 17718	17585466+6747368	K2 III	0.161	6.409	6.306	6.428	6.389	6.348
NPM1p68.0422	◁	BD +68°1022	18471980+6816448	K2 III	0.462	6.816	6.712	6.822	6.780	6.742

[a] The star names used in this project are either abbreviated R.A.-only 2MASS designations, the designation NPM1 from the Lick Northern Proper Motion program (Klemola et al. 1987), with "p" replacing +, or the designation KF from a north ecliptic pole optical/near-infrared survey (Kümmel & Wagner 2000). These are not intended to replace the formal designations.

[b] Designation of the corresponding 2MASS catalog entry, with "2MASSJ" prefix removed, comprising the J2000.0 right ascension and declination sans punctuation (2 decimal places of seconds of right ascension and one decimal place of arcseconds of declination).

All calibration star observations are performed by placing the star in five positions: the center of the array and the centers of the four quadrants of the array. A single frame is taken at each position. Exposure times are set to place the peak brightness at approximately 1/3 of saturation, so that the signal-to-noise ratio is high and the nonlinearity corrections are accurate. The IRAC arrays saturate at $\sim 10^5$ e or 40,000 DN (whichever is lower).

3. PHOTOMETRY

As input, we use the Basic Calibrated Data (BCD) generated by the IRAC science pipeline (ver. S10[4]). In short, the pipeline removes the electronic bias, subtracts a dark sky image generated from observations of relatively empty sky near the ecliptic pole, flat-fields using a "superflat" generated from the first year's calibration observations of relatively blank fields near the ecliptic plane, and linearizes using laboratory measurements of each pixel's response to a calibration lamp, in frames of varying length. For each BCD image in each standard-star observation, aperture photometry was used to determine the source flux. The target is located as the image maximum after spatial filtering (low-pass, median, 7 pixel width) to reduce noise and cosmic rays; this filtered image was used *only* for source identification. (Some of the candidate calibrators observed during in-orbit checkout have other stars nearby; they were located using the coordinates of the star and the astrometric calibration of the images.) The target location is then refined using a centroiding algorithm (`cntrd` in IDLPHOT). We convert the image into electron units for proper error estimation: from the pipeline-processed images (which are in MJy sr^{-1}), we multiply by the gain (`GAIN` in the header; e DN^{-1})

and exposure time (`EXPTIME` in the header) and divide by the calibration factor (`FLUXCONV` in the header; MJy sr^{-1} DN^{-1} s) that had been used in the pipeline; the scaled image at pixel i, j is then I_{ij} in electrons. To get the absolute brightness of each pixel, we also added the brightness of the zodiacal light at the time of the sky-dark observation (approximately 0.036, 0.18, 1.6, and 4.4 MJy sr^{-1} in channels 1, 2, 3, and 4, respectively); this is only important for error propagation, as it is a constant over the image. The background is calculated by a robust average in an annulus spanning a 12 to 20 pixel radius centered on the target:

$$I_{\text{sky}} = \Sigma_{\text{sky}}^{\text{robust}} I_{ij}/N_{\text{sky}}. \tag{1}$$

The on-source flux is calculated by summing over a 10 pixel radius centered on the target (`aper` in IDLPHOT):

$$F_{\text{elec}} = \Sigma_{\text{on}} I_{ij} - I_{\text{sky}}. \tag{2}$$

The electron production rate, $N_e = F_{\text{elec}}/t$, is proportional to the stellar flux.

An array-location–dependent photometric correction must be applied to IRAC photometry to account for the variation in pixel solid angle (due to distortion) and the variation of the spectral response (due to the tilted filters and wide field of view) over the array (J. Hora et al. 2005, in preparation). The photometric corrections are defined to be unity in the center of the array, so their role in the data analysis here is to remove a systematic error that would make the calibration stars, which were observed at five widely separated positions on the array (see Table 4 for the exact locations), have dispersions significantly higher than the measurement uncertainties. Table 4 shows the percentage corrections that were applied; specifically, if the table entries

are f_{ij}, then the fluxes in channel i at position j were divided by $1 + f_{ij}/100$.

A photometric correction must also be applied to IRAC photometry to account for the variation in the flux of a source as a function of location within a pixel. Sources placed directly in the center of a pixel give higher count rates than those placed near a pixel edge. The effect may be due to a nonuniform quantum efficiency across each pixel. We refer to the "pixel phase" as the distance of the centroid of a star from the center of the pixel containing the centroid. The pixel-phase corrections are normalized such that randomly placed sources will have equal chances of requiring an increase or decrease in the flux. For randomly placed sources, this location is $1/\sqrt{2\pi}$ pixels from the center. The pixel-phase dependence is only clearly detected in channel 1, and an approximate fit is

$$f_{\text{phase}} = 1 + 0.0535(1/\sqrt{2\pi} - p), \qquad (3)$$

where p is the distance (in pixels) from the source centroid to the center of the pixel containing that centroid. Observed fluxes in channel 1 were divided by f_{phase}. The channel 1 calibration stars tended on average to fall closer to the centers of their pixels than a random distribution, and the median correction $\langle f_{\text{phase}} \rangle = 1.0\%$.

The photometric uncertainty estimate includes three terms. First, the uncertainty in the subtracted sky background is the rms of the pixel values in the sky annulus, σ_{sky}, divided by the square root of the number of pixels in the sky annulus, and multiplied by the number of on-target aperture pixels:

$$\sigma_{\text{sky}} = \mathcal{R}_{\text{sky}} N_{\text{on}}/\sqrt{N_{\text{sky}}}, \qquad (4)$$

where $\mathcal{R}_{\text{sky}}$ denotes the rms intensity in the sky annulus. Second, noise due to sky variations within the on-source aperture is

$$\sigma_{\text{sky, on}} = \mathcal{R}_{\text{sky}}\sqrt{N_{\text{on}}}. \qquad (5)$$

And third, the Poisson noise on the total background-subtracted counts within the on-source aperture is

$$\sigma_{\text{Poisson}} = \sqrt{F_{\text{elec}}}. \qquad (6)$$

The uncertainty in the flux is then the quadrature sum of the three error terms:

$$\sigma_F = \sqrt{\sigma_{\text{sky}}^2 + \sigma_{\text{sky, on}}^2 + \sigma_{\text{Poisson}}^2}. \qquad (7)$$

We have not explicitly included random variations in the instrument or its calibration. Instead, we attempt to measure those variations through the dispersion in photometry on a large number of images. All three terms in equation (7) contribute significantly to the photometric uncertainty. For example, for NPM1p64.0581, the proportion $\sigma_{\text{sky}} : \sigma_{\text{sky, on}} : \sigma_{\text{poisson}}$ is

TABLE 2
IRAC CALIBRATOR CANDIDATES

Star[a]	Type	R.A. (J2000.0)	Decl. (J2000.0)	Channels
1732526	A3 V	17 32 52.6	+71 04 43.1	1, 2, 3
1739431	A3 V	17 39 43.2	+61 02 55.8	1, 2, 3, 4
1740346	A5 V	17 40 34.7	+65 27 15.0	1, 2, 3, 4
1743045	A5 V	17 43 04.5	+66 55 01.7	1, 2, 3, 4
1757132	A3 V	17 57 13.2	+67 03 40.0	1, 2, 3, 4
1802271	A3 V	18 02 27.2	+60 43 35.6	1, 2, 3, 4
1805292	A1 V	18 05 29.3	+64 27 52.1	1, 2, 3, 4
1808347	A3 V	18 08 34.8	+69 27 28.7	1, 2, 3, 4
1812095	A2 V	18 12 09.6	+63 29 42.3	1, 2, 3, 4
1812523	A1 V	18 12 52.4	+60 02 32.0	1, 2, 4
KF01T3	K1 III	18 03 45.5	+66 56 03.0	1, 2, 3, 4
KF01T5	K1 III	18 04 03.8	+66 55 43.0	1, 2, 3, 4
KF02T1	K0 III	18 02 01.7	+66 37 39.0	1, 2, 3, 4
KF02T3	K0 III	18 03 21.8	+66 34 08.0	1, 2, 3, 4
KF03T1	K0 III	17 57 43.9	+66 26 55.0	1, 2, 3, 4
KF03T2	K1.5 III	17 57 51.4	+66 31 03.0	1, 2, 3, 4
KF03T4	K1 III	17 59 03.9	+66 30 59.0	1, 2, 3, 4
KF05T1	K1 III	17 59 12.1	+66 41 36.0	1, 2, 3, 4
KF06T1	K1.5 III	17 57 58.5	+66 52 29.0	1, 2, 3, 4
KF06T2	K1.5 III	17 58 37.9	+66 46 52.0	1, 2, 3, 4
KF06T3	K1 III	17 58 50.2	+66 49 40.0	1, 2, 3, 4
KF07T2	K1.5 III	18 01 40.7	+65 59 44.0	1, 2, 3, 4
KF07T3	K1.5 III	18 02 14.8	+66 03 00.0	1, 2, 3, 4
KF08T3	K0.5 III	17 55 16.2	+66 10 11.0	1, 2, 3, 4
KF09T1	K0 III	17 59 23.0	+66 02 56.0	1, 2, 3, 4
NPM1p61.0569	K0.5 III	17 23 25.9	+61 12 40.7	1, 2, 3, 4
NPM1p61.0570	K1 III	17 26 11.6	+61 00 48.1	1, 2, 3, 4
NPM1p61.0582	K1 III	17 36 55.6	+61 40 58.1	1, 2, 3, 4
NPM1p64.0590	K0 III	19 25 14.9	+65 01 58.9	1, 2, 3, 4
NPM1p66.0507	K2 III	17 31 22.1	+66 46 35.3	1, 2, 3, 4
NPM1p66.0513	K2 III	17 43 53.7	+66 31 49.8	1, 2, 3, 4
NPM1p66.0514	K0.5 III	17 45 45.4	+66 48 45.4	1, 2, 3, 4
NPM1p67.0536	K2 III	17 58 54.5	+67 47 37.4	1, 2, 3, 4
NPM1p68.0412	K2 III	18 28 24.8	+68 58 51.5	1, 2, 3, 4

[a] The star names used in this project are either abbreviated R.A.-only 2MASS designations, the designation NPM1 from the Lick Northern Proper Motion program (Klemola et al. 1987), with "p" replacing +, or the designation KF from a north ecliptic pole optical/near-infrared survey (Kümmel & Wagner 2000). These are not intended to replace the formal designations.

0.64 : 0.66 : 0.39 for channel 1, 0.71 : 0.54 : 0.45 for channel 2, 0.69 : 0.58 : 0.43 for channel 3, and 0.80 : 0.33 : 0.50 for channel 4. The differences in proportion are due to background brightness and dispersion, source flux, and exposure time in each channel. The value for σ_{sky} can be reduced somewhat by increasing the size of the sky annulus. Both $\sigma_{\text{sky, on}}$ and σ_{sky} can be reduced by decreasing the size of the on-source aperture, but then we would lose some flux and require larger aperture corrections. The choice of on-source and sky apertures used here is optimized for calibration purposes, where we attempt to gather as much of the star's flux as possible. For source detection, a smaller on-source aperture is recommended. All of the calibration stars are bright; for example, for NPM1p64.0581, the flux-to-uncertainty ratio (F/σ_F) is 158, 106, 123, and 96 for channels 1, 2, 3, and 4, respectively, in a single BCD image.

The flux and photometric uncertainty were calculated for

TABLE 3
IRAC Secondary Calibrators for Each Campaign

Number	Campaign	Star	R.A. (J2000.0)	Decl.	Type	[3.6]	[4.5]	[5.8]	[8.0]
1	IRAC003500	HD 218528	23 08 49.4	−08 48 27	K0 III	6.311 ± 0.025	6.367 ± 0.045	6.361 ± 0.024	6.309 ± 0.021
		SA 115-554	23 41 31.0	+01 26 26	K1.5 III	9.071 ± 0.021	9.213 ± 0.025	9.154 ± 0.018	9.099 ± 0.019
2	IRAC003600	HD 4182	00 44 25.4	+09 57 09	A2 V	8.990 ± 0.021	8.981 ± 0.021	8.974 ± 0.021	8.980 ± 0.021
		SA 115-554	23 41 31.0	+01 26 26	K1.5 III	9.071 ± 0.021	9.213 ± 0.025	9.154 ± 0.018	9.099 ± 0.019
3	IRAC003700	BP 20 417	02 32 14.4	+20 49 09	K1.5 III	7.777 ± 0.022	8.058 ± 0.025	7.998 ± 0.018	7.944 ± 0.018
4	IRAC003800	BP 14 549	03 18 20.3	+15 25 41	K2 III	7.104 ± 0.021	7.234 ± 0.027	7.192 ± 0.018	7.138 ± 0.019
5	IRAC003900	HD 37725	05 41 54.4	+29 17 51	A3 V	7.876 ± 0.023	7.870 ± 0.023	7.864 ± 0.023	7.869 ± 0.023
		HD 244937	05 34 54.2	+30 03 28	A1 V	8.512 ± 0.023	8.488 ± 0.023	8.472 ± 0.023	8.487 ± 0.023
6	IRAC004000	HD 55728	07 14 47.6	+16 35 50	A2 V	9.465 ± 0.019	9.464 ± 0.019	9.461 ± 0.020	9.463 ± 0.020
		HD 55677	07 14 31.3	+13 51 37	A4 V	9.189 ± 0.020	9.187 ± 0.02	9.184 ± 0.020	9.187 ± 0.020
7	IRAC004100	AKS 95 408	08 48 52.6	+19 03 42	K0 III	9.187 ± 0.020	8.511 ± 0.044	8.505 ± 0.023	8.453 ± 0.019
		HD 77823	09 05 15.8	+14 14 43	K1.5 III	6.183 ± 0.021	6.325 ± 0.025	6.266 ± 0.018	6.211 ± 0.018
8	IRAC004200	HD 89562	10 20 08.9	+03 11 56	K0 III	6.949 ± 0.025	7.004 ± 0.045	6.998 ± 0.024	6.946 ± 0.021
		HD 90593	10 27 44.2	+04 28 20	K0 III	7.049 ± 0.026	7.105 ± 0.045	7.099 ± 0.025	7.047 ± 0.023
9	IRAC004800	HD 99253	11 25 14.9	−05 52 08	K1.5 III	6.239 ± 0.022	6.381 ± 0.026	6.322 ± 0.020	6.267 ± 0.020
10	IRAC004900	HD 109441	12 34 47.7	−11 46 47	K0 III	7.123 ± 0.024	7.179 ± 0.044	7.173 ± 0.024	7.121 ± 0.021
		HD 113745	13 05 57.0	−08 41 33	A0 V	8.835 ± 0.020	8.832 ± 0.02	8.829 ± 0.020	8.834 ± 0.020
11	IRAC005000	HD 131769	14 55 51.2	−12 12 28	K1.5 III	6.552 ± 0.022	6.682 ± 0.026	6.616 ± 0.019	6.567 ± 0.020
		HD 135248	15 14 21.4	−08 50 39	K1 III	6.596 ± 0.022	6.704 ± 0.032	6.663 ± 0.021	6.611 ± 0.022
12	IRAC005100	HD 137429	15 26 29.7	−14 28 35	K0 III	6.181 ± 0.027	6.227 ± 0.046	6.217 ± 0.026	6.169 ± 0.023
		HD 145152	16 09 51.2	−12 19 09	K2 III	6.570 ± 0.024	6.705 ± 0.029	6.666 ± 0.022	6.609 ± 0.022
13	IRAC005200	HD 155334	17 12 01.2	−25 40 54	A1 V	7.716 ± 0.022	7.714 ± 0.022	7.710 ± 0.023	7.714 ± 0.023
		HD 156896	17 20 55.5	−20 21 35	A0 V	9.364 ± 0.021	9.355 ± 0.021	9.349 ± 0.021	9.357 ± 0.021
14	IRAC005300	HD 184837	19 37 16.4	−24 40 11	A0 V	9.595 ± 0.021	9.587 ± 0.021	9.581 ± 0.021	9.588 ± 0.021
15	IRAC005400	HD 195061	20 29 33.2	−18 13 12	A0 V	9.330 ± 0.022	9.318 ± 0.022	9.310 ± 0.022	9.319 ± 0.022

each image of each calibration star; 15,341 fluxes were measured for IRAC campaigns 1–15.

4. PHOTOMETRIC STABILITY

To monitor the stability of the camera on various timescales, the primary and secondary calibrators were all reduced uniformly and plotted together. Figures 1–5 show the results for five IRAC nominal operations campaign.

4.1. Stability on Weekly Timescales

The relative repeatability of IRAC was measured by taking the rms variations of each secondary calibration star photometry during a campaign. The distribution of these variances among all of the campaigns has a χ^2 probability distribution function. The median of these rms values is 1.7%, 2.2%, 1.5%,

TABLE 4
Array-Location–Dependent Photometric
Corrections (%)

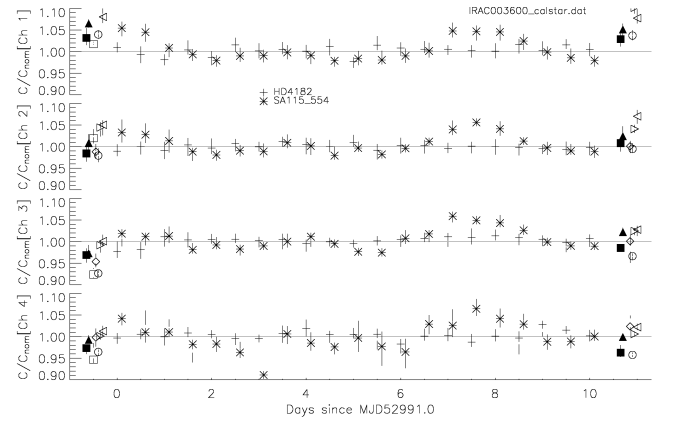| Index	Column	Row	Channel			
			1	2	3	4
0	128	128	0.00	0.00	0.00	0.00
1	64	192	0.52	0.53	3.86	−1.31
2	192	192	0.46	1.75	−0.85	1.50
3	192	64	1.34	1.56	−1.63	2.66
4	64	64	1.34	0.68	3.39	−0.39

Fig. 1.—Summary of calibration star results during the second IRAC campaign of the routine science mission. Each point is a measurement of the absolute calibration factor, normalized by the new calibration factors derived in this paper (0.1104, 0.1390, 0.6024, 0.2083 [MJy sr^{-1}]/[DN s^{-1}]). The clusters of points and the beginning of each plot are the primary calibrators, which always have the same symbol type in each plot. Filled symbols indicate A dwarfs, and open symbols show K giants. Symbols for the primary calibrators are the same as in the second column of Table 1. Two error bars are shown for each point, indicating the rms dispersion and the uncertainty in the mean. Spread throughout each campaign are the secondary calibrators, observed every 12 hr. One or more secondary calibrators are observed each campaign, with source names indicated in a legend for each campaign. One of the two secondary calibrators (SA 115-554) is apparently a variable star and has been removed from our calibrator list.
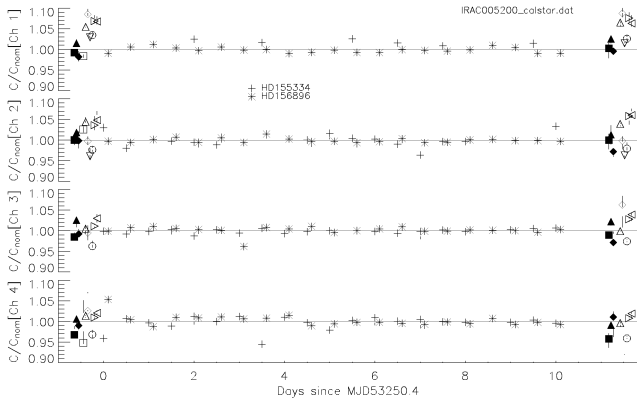
Fig. 4.—Same as Fig. 1, but for campaign IRAC005200.

Fig. 2.—Same as Fig. 1, but for campaign IRAC004100.

and 1.6% in channels 1, 2, 3, and 4, respectively. The variance of the rms is consistent with the median photometric measurement error, which is 0.5%, 0.9%, 0.7%, and 0.9% in channels 1, 2, 3, and 4, respectively. Some stars have higher dispersions, but only one star at one wavelength (compared to a total of 20 stars at four wavelengths) has an rms dispersion larger than 5%. This is a measure of the repeatability of pho-

tometry within a campaign, which can be summarized as being stable to 2%.

4.2. Stability on Long Timescales

The camera is evidently stable on all timescales that have been checked. Table 5 summarizes the statistics characterizing the long-term stability for eight primary calibrators over 11 months.

To assess the stability, we use the statistics for individual calibrators in Table 5. Normalizing the count rates for each primary calibrator by their median, the long-term dispersion in the photometry becomes 1.7%, 0.9%, 0.9%, and 0.5% in channels 1, 2, 3, and 4, respectively.

To determine whether the photometry has significant long-term variations (due to source or instrument), we inspected the
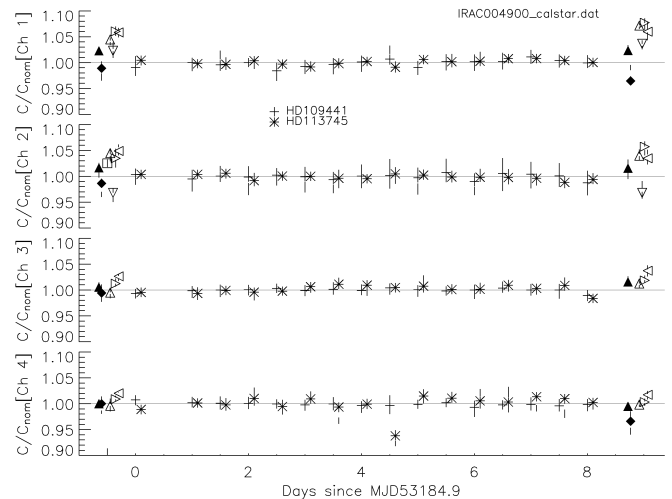

Fig. 5.—Same as Fig. 1, but for campaign IRAC005400. This campaign length is typical of the second year of routine operations.

Fig. 3.—Same as Fig. 1, but for campaign IRAC004900.

TABLE 5
Long-Term (1 yr) Stability of IRAC Primary Calibration Stars

Star	Channel	Median[a]	rms[b]	WTmean[c]	WTsig[d]	Slope[e]	Sigslope[e]
NPM1p64.0581	1	0.9672	0.0163	0.9709	0.0024	−0.01246	0.006787
NPM1p64.0581	2	1.0105	0.0099	1.0071	0.0029	0.00316	0.004725
NPM1p64.0581	3	1.0080	0.0082	0.9970	0.0012	0.00651	0.003850
NPM1p64.0581	4	1.0017	0.0125	1.0081	0.0024	0.00142	0.005372
HD 165459	1	0.9892	0.0192	0.9815	0.0004	−0.01192	0.008299
HD 165459	2	1.0269	0.0067	1.0253	0.0020	−0.00212	0.002973
HD 165459	3	1.0412	0.0083	1.0422	0.0008	0.00366	0.003180
HD 165459	4	1.0390	0.0053	1.0373	0.0012	0.00127	0.002308
NPM1p60.0581	1	0.9513	0.0124	0.9497	0.0018	−0.00802	0.007658
NPM1p60.0581	2	0.9931	0.0183	1.0205	0.0008	−0.01825	0.010200
NPM1p60.0581	3	1.0018	0.0828	0.9933	0.0020	−0.01570	0.010688
NPM1p60.0581	4	1.0295	0.0178	1.0208	0.0020	0.00867	0.011478
KF09T1	1	1.0268	0.0082	1.0292	0.0010	0.00806	0.005187
KF09T1	2	1.0510	0.0073	1.0521	0.0017	0.00285	0.004707
KF09T1	3	1.0195	0.0069	1.0178	0.0011	0.01244*	0.003559*
KF09T1	4	1.0424	0.0079	1.0470	0.0011	0.00365	0.005214
KF06T1	1	1.0621	0.0241	1.0736	0.0019	−0.02734	0.011175
KF06T1	2	1.0081	0.0083	1.0086	0.0018	−0.00551	0.003902
KF06T1	3	1.0174	0.0643	1.0072	0.0055	0.04192	0.024166
KF06T1	4	1.0648	0.0323	1.0745	0.0048	0.02743	0.014229
NPM1p66.0578	1	1.0004	0.0143	0.9971	0.0004	−0.00989	0.006577
NPM1p66.0578	2	0.9934	0.0096	0.9993	0.0019	−0.00448	0.004144
NPM1p66.0578	3	0.9869	0.0081	0.9853	0.0013	0.00651	0.003476
NPM1p66.0578	4	0.9986	0.0043	1.0010	0.0008	−0.00018	0.002175
NPM1p67.0536	1	1.0351	0.0176	1.0295	0.0014	0.00070	0.007963
NPM1p67.0536	2	1.0507	0.0097	1.0558	0.0025	0.00085	0.004416
NPM1p67.0536	3	1.0383	0.0092	1.0374	0.0014	0.00062	0.004163
NPM1p67.0536	4	1.0470	0.0044	1.0463	0.0010	0.00253	0.001915
NPM1p68.0422	1	1.0349	0.0170	1.0336	0.0014	−0.01374	0.007078
NPM1p68.0422	2	1.0697	0.0122	1.0667	0.0027	−0.00912	0.004984
NPM1p68.0422	3	1.0497	0.0077	1.0496	0.0017	0.00767	0.003115
NPM1p68.0422	4	1.0605	0.0057	1.0597	0.0010	0.00180	0.002322

[a] Median of calibration factors measured in each of the first 11 campaigns, normalized to nominal values 0.1104, 0.1390, 0.6024, 0.2083 (MJy sr^{-1})/(DN s^{-1}) for channels 1, 2, 3, and 4, respectively.

[b] The rms of normalized calibration factors.

[c] Weighted mean of normalized calibration factors, with the weight for each point being the rms dispersion of measurements during a campaign.

[d] Formal statistical uncertainty in the weighted mean of the normalized calibration factors.

[e] Least-squares–fitted slope (and its statistical uncertainty) for the normalized calibration factors, in units of fractional variation per year. Apparently statistically significant slopes are indincated with asterisks (*).

long-term trends for each calibrator. Figure 6 shows the trend of the count rates over the first 11 months of the mission, and the last two columns in Table 5 show least-squares–fitted slopes to the temporal variations. An instrumental trend will be the same for each primary calibrator, while stellar variability will appear only in the individual star. Measurement errors generate dispersion (both random and systematic) that should not correlate between stars. Only one (KF09T1, channel 3) of the 32 (eight calibrators, four channels) trend plots shows a slope that is formally significant.[5] The other primary calibrators are all stable at a level of <1.5% yr^{-1}.

5. ABSOLUTE CALIBRATION

5.1. Flux Prediction for Primary Calibrators

For each primary calibrator, we predicted the count rate in each IRAC channel. The procedure was explained in detail by Cohen et al. (2003). In brief, the spectral type of each star was determined from ground-based visible spectroscopy (Megeath et al. 2003). The intrinsic spectral energy distribution for that type was determined from models for the A stars (Kurucz 1993a, 1993b) or from empirical spectral templates derived from observations for the K giants (Cohen et al. 1996). For

[5] This example shows how a simple monitoring program with observations of five frames each every 10–20 days can limit variability at the 2% level.

Such a monitoring program takes approximately 2 hr of observing time per year, including slews to the target and observing at all four wavelengths.
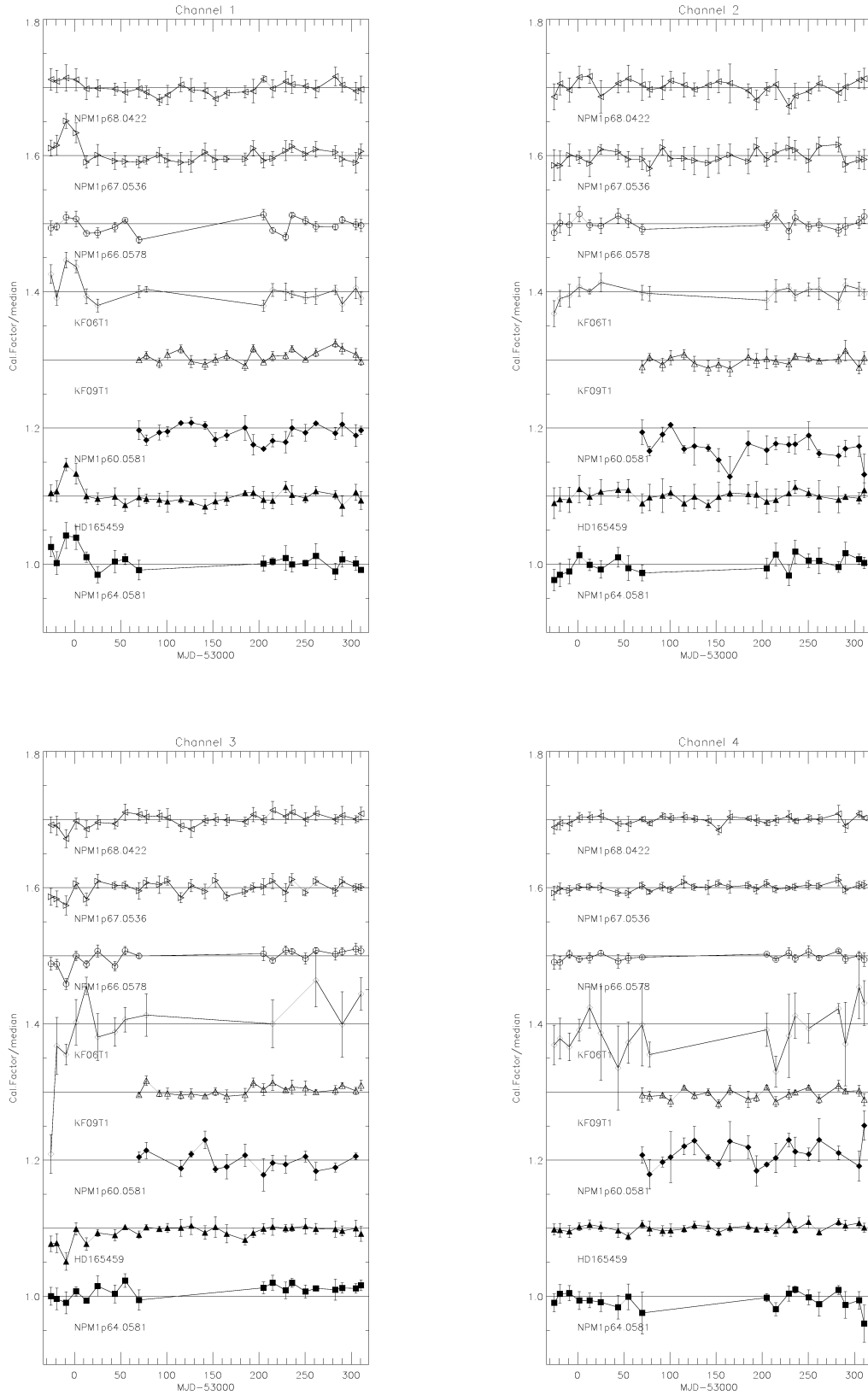
FIG. 6.—Long-term monitoring of the calibration factor derived from individual primary calibrators. Each panel is for a different IRAC channel: 1 (*top left*), 2 (*top right*), 3 (*bottom left*), and 4 (*bottom right*). Within each panel, the calibration factors for each primary calibrator have been normalized to their median, and they have been offset from the previous curve by 0.1.

TABLE 6
PREDICTED BRIGHTNESS OF PRIMARY ABSOLUTE CALIBRATORS

NUMBER	STAR	PREDICTED FLUX, $F_{\nu_0}^* K^*$ (mJy)[a]				CAMPAIGN LOG
		3.6 μm	4.5 μm	5.8 μm	8.0 μm	
1	NPM1p64.0581	63.03 $\pm$ 1.49	41.03 $\pm$ 0.95	26.17 $\pm$ 0.62	14.40 $\pm$ 0.34	yyyyyynnnny
2	HD 165459	647.38 $\pm$ 17.02	421.19 $\pm$ 10.85	268.71 $\pm$ 7.06	148.09 $\pm$ 3.90	yyyyyyyyyyy
3	NPM1p60.0581	38.20 $\pm$ 0.89	24.74 $\pm$ 0.56	15.75 $\pm$ 0.37	8.70 $\pm$ 0.20	nnnnyyyyyyy
4	1812095	8.68 $\pm$ 0.20	5.66 $\pm$ 0.12	3.62 $\pm$ 0.08	2.00 $\pm$ 0.04	yyyyyyyyyyy
5	KF08T3	11.78 $\pm$ 0.42	7.25 $\pm$ 0.45	4.64 $\pm$ 0.13	2.69 $\pm$ 0.08	yyyyyyyyyyy
6	KF09T1	169.94 $\pm$ 5.86	104.69 $\pm$ 6.33	67.02 $\pm$ 1.74	38.76 $\pm$ 1.04	ynnnyyyyyyy
7	KF06T1	13.93 $\pm$ 0.46	7.80 $\pm$ 0.50	5.34 $\pm$ 0.13	3.09 $\pm$ 0.08	yyyyyynnnny
8	KF06T2	10.53 $\pm$ 0.35	5.99 $\pm$ 0.38	4.05 $\pm$ 0.10	2.34 $\pm$ 0.06	nnnnyyyyyyy
9	NPM1p66.0578	140.94 $\pm$ 6.11	82.39 $\pm$ 7.34	54.54 $\pm$ 1.60	29.72 $\pm$ 1.03	yyyyyynnnny
10	NPM1p67.0536	843.49 $\pm$ 35.09	482.35 $\pm$ 39.32	319.84 $\pm$ 9.81	185.25 $\pm$ 7.39	yyyyyyyyyyy
11	NPM1p68.0422	580.54 $\pm$ 24.89	335.64 $\pm$ 27.73	223.18 $\pm$ 7.01	128.96 $\pm$ 5.22	yyyyyyyyyyy

[a] Predicted flux density in "quoted" IRAC convention. The predicted flux density at the nominal wavelength is $F_{\nu_0}^*$, and the color correction for each star's predicted spectrum spectrum is K^*.

each star, an absolute normalization and the extinction A_V were derived by fitting the intrinsic SED to optical (*UBV*, *Hipparcos* H_p, Tycho-2 B_T and V_T), near-infrared (Two Micron All Sky Survey—2MASS), and mid-infrared (*IRAS*, *MSX*) photometry. Table 1 shows the 2MASS J, H, and K_S magnitudes (Skrutskie 1999) and the derived extinction for each primary calibrator.

The reddened stellar SED template for each primary calibrator gives its flux density at all wavelengths on a scale consistent with the network of standards constructed by Cohen et al. (1999) and absolutely validated by Price et al. (2004). The fluxes in the IRAC wavebands were calculated by integrating the normalized spectral template for each star over the IRAC spectral response. The detailed derivation of the calibration factors is as follows. The number of electrons per unit of time collected from a source with spectrum F_ν using a telescope with area A is

$$N_e = A \int \frac{F_\nu}{h\nu} R \, d\nu, \qquad (8)$$

where R is the system spectral response (in units of electrons per photon, at frequency ν, determined from prelaunch measurements). The calibration factor is the ratio of the flux density at the nominal wavelength, $\lambda_0 = c/\nu_0$ if the source had the nominal $\nu F_\nu = $ constant spectrum, to the observed electron production rate:

$$C' = \frac{F_{\nu_0}^* K^*}{N_e}, \qquad (9)$$

where the color correction

$$K \equiv \frac{\int (F_\nu/F_{\nu_0}) (\nu/\nu_0)^{-1} R \, d\nu}{\int (\nu/\nu_0)^{-2} R \, d\nu}. \qquad (10)$$

For an imager like IRAC, we calibrate in units of surface brightness, and the flux measurements are made using aperture photometry in a finite aperture that does not necessarily include all of the flux. We continue to use F_ν as the true source spectrum, and we define the calibration factor such that after performing both aperture and color corrections to the observations, the best measurement of the source flux is obtained. To convert from raw IRAC units of data numbers (DN) into surface brightness per pixel, the calibration factor is

$$C = C' \frac{G}{f_{\rm ap} \Omega_{\rm pix}} = \frac{F_{\nu_0}^* K^* G}{f_{\rm ap} N_e \Omega_{\rm pix}}, \qquad (11)$$

where G is the gain (e DN^{-1}), $\Omega_{\rm pix}$ is the pixel solid angle (pixels are square, with 1″22 sides), and $f_{\rm ap}$ is the aperture correction factor (taken to be unity; see § 5.5). The units of the calibration factor C are (MJy sr^{-1})/(DN s^{-1}). The asterisk (*) indicates that the quantity refers to a calibration star, rather than a generic spectrum. It is perhaps worth emphasizing that the only properties of the stellar spectra that enter into the absolute calibration are the integrated in-band fluxes for each IRAC channel, and that the calibration factors are directly proportional to the in-band flux.

Table 6 shows the predicted fluxes of the IRAC primary calibrators. The flux predictions, $F_{\nu_0}^* K^*$, are in IRAC "quoted" units, such as would be obtained from science products from the SSC data analysis pipelines. The monochromatic flux at the nominal wavelength can be determined (for the calibrators or for any pipeline-processed IRAC data) by dividing the quoted flux by the color correction (eq. [10]). The nominal wavelengths for the IRAC bands were chosen to minimize the color corrections. One can show (by making a Taylor series expansion of the source spectrum) that the minimal dependence of the color correction on the slope of the source spectrum is

obtained for the nominal wavelength, defined as

$$\lambda_0 = \frac{\int \lambda \nu^{-1} R \, d\nu}{\int \nu^{-1} R \, d\nu} . \quad (12)$$

The nominal wavelengths calculated in this way, using the current spectral response curves (Fazio et al. 2004), are 3.550, 4.493, 5.731, and 7.872 μm in channels 1, 2, 3, and 4, respectively. Figure 7 shows the model spectra for an A dwarf and K giant calibrator, together with the spectral responses. We calculated the calibrator color corrections K^* separately for each calibrator spectrum. For reference, the color corrections are (in channels 1, 2, 3, and 4, respectively), for an A1 V star: $K_A^* = 1.019$, 1.001, 1.026, and 1.042; for an K1.5 III star: $K_K^* = 1.021$, 1.070, 1.001, and 1.093; and for Rayleigh-Jeans spectra: $K_{RJ} = 1.011$, 1.012, 1.016, and 1.034.

The IRAC spectral response calibration convention, such that no color corrections are needed for sources with $\nu F_\nu =$ constant spectra, is essentially the same convention used by *IRAS* (Beichman et al. 1988), *COBE* DIRBE (Hauser et al. 1998), and *ISO* (Blommaert et al. 2003), except that the monochromatic flux densities are at the nominal wavelength (eq. [12]) for each channel, rather than at a round-number wavelength.

5.2. Comparison of Different Standard Stars

To search for systematic trends in the comparison of observed and predicted fluxes, we used two samples: the primary standard stars selected for the nominal mission (11 stars; Table 1) and the candidate calibrators observed during the in-orbit checkout (34 stars; Table 2). The primary standards defined the IRAC calibration, so we consider the candidate calibrators as a relatively independent comparison sample to search for trends. Figure 8 shows the histograms of the predicted/observed fluxes for the candidate calibrators, for each IRAC channel. The "observed" fluxes have been scaled using the calibration factors averaged over the primary standards in the method described below in § 5.3. The distributions are centered near unity, demonstrating good agreement between the candidate calibrator and primary standards.

We found one systematic trend in the predicted/observed fluxes: a displacement between the calibration derived from A dwarfs and K giants, in IRAC channels 1 and 2. Figure 8 shows the histogram of the calibration factors separately for these two types of primary calibrators. The difference in average calibration inferred from the two types of calibrators is twice as large as the widths (3.4%) of the distributions for each calibrator type. This leads to an unnecessary systematic error in the calibration, with a spectral dependence that changes channels 1 and 2 with respect to the other IRAC channels. To bolster the statistics, we include the primary standards together with the calibrators observed only in IOC; the total sample comprises 13 A stars and 29 K stars. The difference between the A and K star distributions of predicted/observed fluxes is 7.3% ± 2.3% in channel 1,
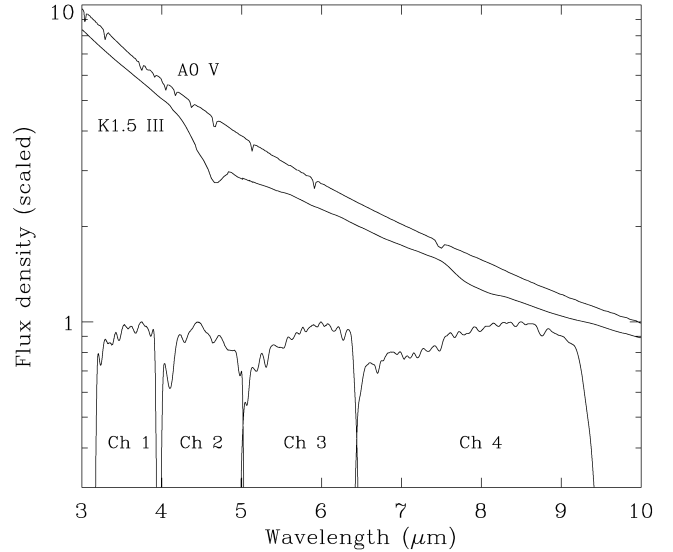

FIG. 7.—Predicted spectra of two primary calibrators, an A dwarf and a K giant, together with the relative spectra responses of the four IRAC channels. Both the spectra (flux density units; ∝Jy) and relative spectral response (in electrons per photon) were scaled arbitrarily to unity to fit on this plot.

6.5% ± 2.4% in channel 2, 3.6% ± 2.5% in channel 3, and 2.1% ± 2.8% in channel 4, with the predicted/observed fluxes higher for K stars than for A stars in all four channels. Our original calibration strategy was to observe both A and K calibrators, then take the average to guard against model uncertainties. After seeing such a clear systematic difference, with a color dependence, between the two types of calibrators, and furthermore, seeing that there is no temporal drift in the calibration (so that we can use all calibration star data all the way back to the in-orbit checkout), we decided to adopt an A-star–only absolute calibration convention. At present, we do not know why the K giants are systematically offset from the A stars, nor do we conclusively know which of the two types of calibration are correct. With the relatively small number of stars observed and analyzed here, and with only two types of calibrators analyzed, it is not possible to conclusively say whether the template spectra are inaccurate representations of the stars, or if the particular sample of stars is anomalous.

The distribution of predicted/observed flux (Fig. 8) is non-Gaussian, because it is a combination of the measurement uncertainties (which do have a Gaussian distribution) and the systematic uncertainties (which do not). In all four IRAC channels (but particularly channel 1), two peaks in the distribution are evident, due to the separate distributions of A and K stars. Furthermore, there are too few calibrators for the central limit theorem to lead to a clean Gaussian distribution for each type. The dispersions of the distributions are ~2.5%–3.5%, which is comparable to the uncertainty in the predicted fluxes based
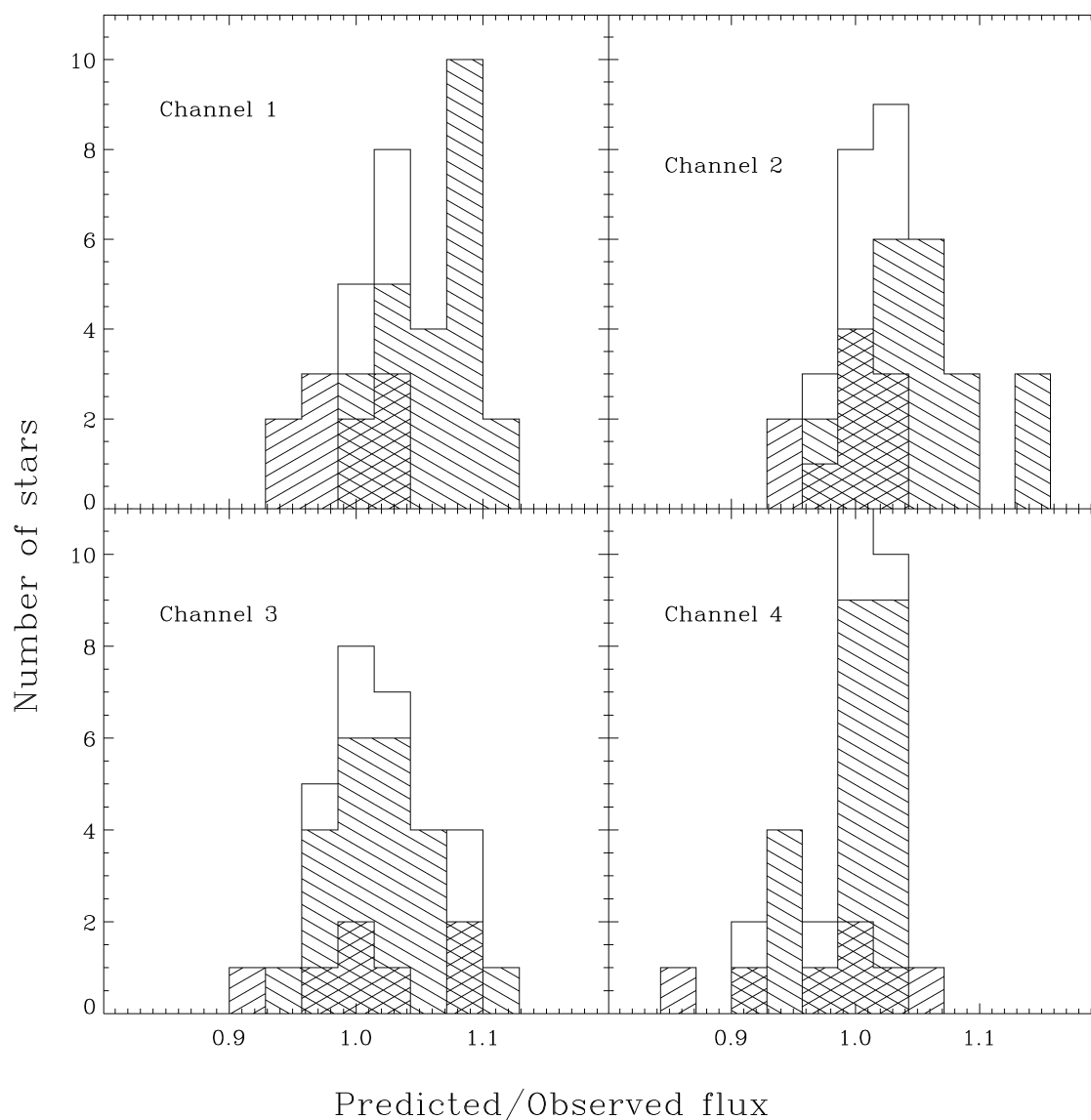
FIG. 8.—Distributions of predicted/observed fluxes for the 34 calibrator candidates in each IRAC channel. Each box represents one star. The histogram of the total sample is the upper envelope. The histogram for A stars only has diagonal hatching one way (/), and the histogram for K stars only has diagonal hatching another way (\). The two distributions overlap near unity, but the displacement is evident, with the K stars having higher predicted than observed flux.

only on prelaunch ground and space measurements with other telescopes.

5.3. Best Calibration Factors and Their Uncertainties

The recommended calibration factors for IRAC were calculated as a weighted average of calibration factors for the four A-type primary calibrators. The results are given in Table 7.[6]

TABLE 7
ABSOLUTE CALIBRATION FACTORS FOR IRAC

Channel	Calibration Factor (MJy sr^{-1})/(DN s^{-1})	σ_{ground} (%)	σ_{rms} (%)	σ_{repeat} (%)
1	0.1088 ± 0.0022	2.3	2.0	0.9
2	0.1388 ± 0.0027	2.3	1.9	0.9
3	0.5952 ± 0.0121	2.3	2.1	0.9
4	0.2021 ± 0.0041	2.3	2.1	0.8

---

[6] The calibration factors in Table 7 have been applied to IRAC data with pipeline ver. S11.

Weights were inversely proportional to the uncertainties in the absolute calibration of each star (Cohen et al. 2003).

The total uncertainty in the calibration factor is *not* the statistical uncertainty in the weighted mean, since $\sigma_{abs} = 1.5\%$ of the uncertainty in each of the predicted fluxes arises from the absolute calibration of Vega and Sirius, which scales all of the predictions. To assess the uncertainty in the calibration, we separate three items in Table 7. The absolute calibration uncertainty for each star is σ_{ground}. The dispersion in calibration factors derived from an individual star is σ_{rms}, attributed largely to measurement errors. Finally, the campaign-averaged calibration factor for each star and each calibrator has some dispersion from campaign to campaign of σ_{repeat}, which limits long-term drifts (which are apparently not present for IRAC). The combined uncertainty for n calibrators is determined from

$$\sigma_C = \sqrt{\sigma_{abs}^2 + (\sigma_{ground}^2 - \sigma_{abs}^2)/n + \sigma_{rms}^2/n}. \qquad (13)$$

We used this equation, with $n = 4$, to derive the uncertainty (2.0% in all four IRAC bands) in the absolute calibration factors listed in Table 7.

Including the larger sample of calibrators observed only during IOC, the calibration differs from the values in Table 7 by -0.9%, -1.1%, -1.7%, and -2.3%, respectively, in channels 1, 2, 3, and 4. This difference is marginally significant, and we incorporate it into the overall calibration uncertainty. The IRAC calibration will be updated in future to include these results and a wider sample of spectral types.

5.4. IRAC Magnitude System

We define the IRAC magnitude system such that an observer measures the flux density F_ν^{quot} of a source from the calibrated images out of the IRAC pipeline, performs image-based corrections (array-location–dependent photometric correction, pixel-phase correction, and aperture correction), and then uses the zero-magnitude flux densities $F_{zero}^{[i]}$ to calculate the magnitude $[i] = 2.5 \log_{10}(F_{zero}^{[i]}/F_\nu^{quot})$, where $i = 3.6$, 4.5, 5.8, and 8 are the four IRAC channels. In this system, there is no need to know the spectral shape of the source, as the magnitude is a measure of the in-band flux relative to that of Vega. The zero-magnitude fluxes were determined by integrating the Kurucz model spectrum of α Lyr over the passbands using the equations above; specifically,

$$F_{zero}^{[i]} = \frac{\int F_\nu \, (\nu/\nu_0)^{-1} \, R^{[i]} \, d\nu}{\int (\nu/\nu_0)^{-2} \, R^{[i]} \, d\nu} . \qquad (14)$$

The resulting zero-magnitude flux densities are 280.9 ± 4.1, 179.7 ± 2.6, 115.0 ± 1.7, and 64.13 ± 0.94 Jy in the [3.6], [4.5], [5.8], and [8] μm channels, respectively. Due to the choice of A dwarfs as the absolute calibrators, this magnitude

convention should yield results on the same scale as used in optical and near-infrared astronomy.

5.5. Aperture Corrections and Extended Emission

All the discussion so far has been based on aperture photometry with a specified beam size and sky annulus (§ 3), and the calibration factors in Table 7 are defined for these parameters. The parameters were optimized for photometry of isolated, bright point sources and will not in general be suitable for other applications. In particular, some of the source flux lands in the sky annulus and is subtracted, while additional flux lands outside the sky annulus and is ignored. Measurements using different beam sizes or sky annuli will need to account for these effects. Therefore,

1. point sources extracted with the same aperture that we used for calibration will get the correct flux (no further aperture correction needed);

2. point sources extracted with other on-source radii or sky annuli can use aperture correction tables as long as they are normalized such that there is no correction for apertures identical to those used in our absolute calibration;

3. point sources extracted using point-spread function fitting should verify that the normalization of the point-spread function would give unity flux if the on-source and sky calibration apertures are applied (i.e., not unity flux for the integral over the entire point-spread function); and

4. extended emission surface brightness will be incorrectly calibrated and will require scaling by the "infinite" aperture correction.

The reason we have not attempted an aperture correction is that the measurements are still under way and the empirically derived values are not well understood. Part of the effect is simple diffraction and could be estimated using, for example, an Airy function determined by the primary mirror size and the filter central wavelength; this effect explains channels 1 and 2. However, in channels 3 and 4, substantially more of the source flux is scattered out of the calibration aperture than can be explained by diffraction theory. This light is thought to be scattered within the detector material. Its distribution, dependence on location of the source in the array, and the ultimate fate of the lost source flux are under investigation. The empirical determination of the aperture corrections will be described by M. Marengo et al. (2005, in preparation). At present we recommend that extended emission (including the basic calibrated data and the image mosaics from the pipeline) be multiplied by the effective aperture correction factors of 0.944, 0.937, 0.772, and 0.737 for channels 1, 2, 3, and 4, respectively.

Three further practical matters have already been mentioned but are worth summarizing here as well.

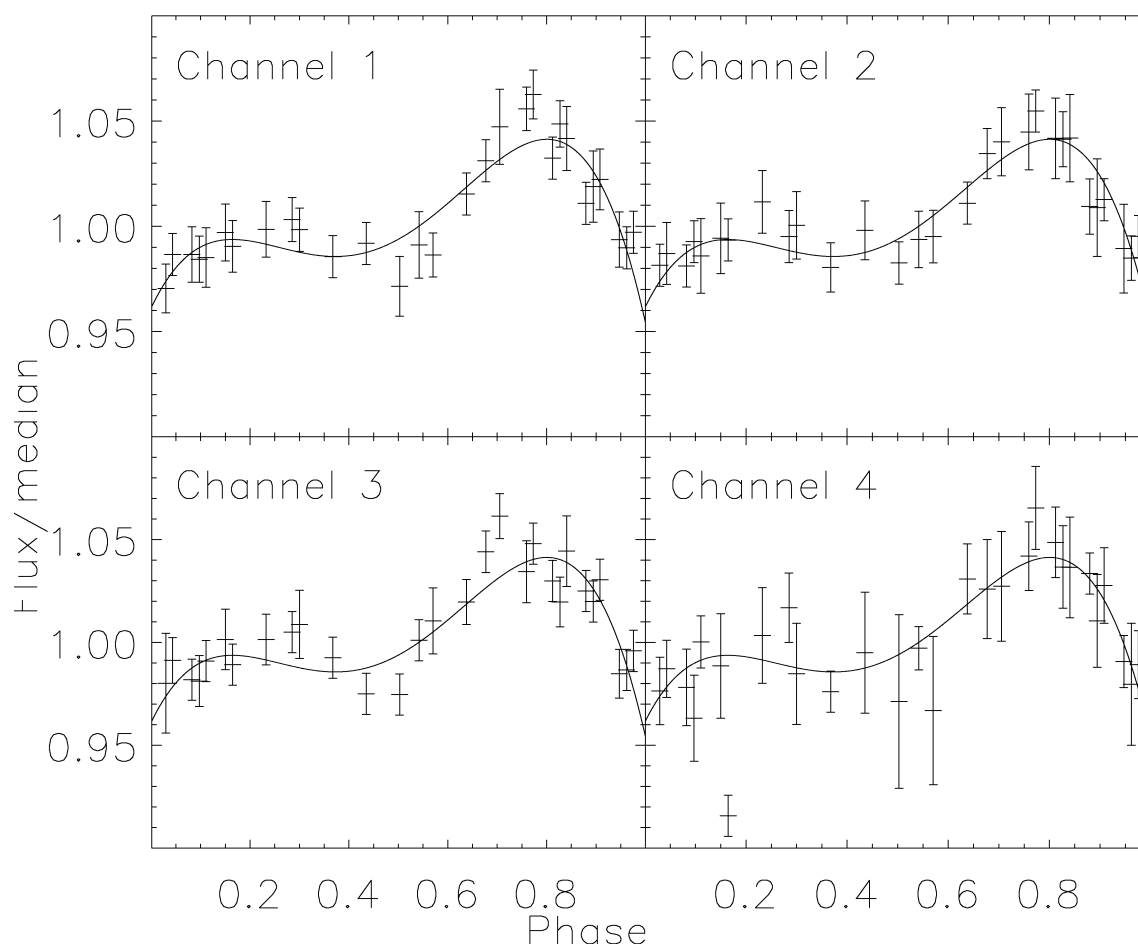1. The IRAC science pipeline generates images in units of

Fig. 9.—Light curve of the secondary calibrator SA 115-554 in the four IRAC channels. The solid curve (same exact curve in each of the four panels) is a fourth-order polynomial fit to all of the wavelengths, indicating the light curve is color-invariant.

surface brightness, but because of distortion, the pixels do not subtend constant solid angle.

2. The IRAC spectral response varies over the field of view, and therefore the color corrections are field dependent.

3. The electron rate in the 3.6 μm channel depends slightly on pixel phase. The present calibration factors are correct on average, as is appropriate for sources observed multiple times at multiple dither positions. For the most precise photometry, however, pixel phase should be taken into account.

Corrections 1 and 2 are available from the *Spitzer* Science Center and are described by J. Hora et al. (2005, in preparation); they were taken into account in the present paper by using the array-location–dependent photometric corrections in Table 4. Correction 3 was applied using the simple equations in § 3. Observers should apply these corrections in a manner consistent with that applied in this paper, in order for the absolute calibration to apply.

6. SERENDIPITOUS RESULTS

The secondary calibrator SA 115-554 has a periodic light curve. It was observed every 12 hr in two campaigns spanning a total of 26 days. The light curve phases well to a period of 7.4 days, with an amplitude of 5%. Figure 9 shows the light curve, phased to 0 at modified Julian Date 52,996.5. The light curve is identical at all four IRAC wavelengths, indicating that the source of variability is not a mid-infrared–specific phenomenon, but rather something with colors comparable to the star, which is classified as a K1.5 III. This star was found to be variable as part of the All Sky Automated Survey (ASAS) by Pojmański (2000), who found *I*-band variability with a period of 7.451 days, identical to the IRAC period. The amplitude of the *I*-band variation was 0.18 mag, and its light curve is distinctly different from that measured by IRAC.

If the variability were due to an orbiting companion, then the companion would probably be late type and small, perhaps

an M dwarf. But the observed variability likely arises from pulsations of the star itself. The optical light curve is more characteristic of a Cepheid variable, and the spectral type obtained by Drilling & Landolt (1979) was G7, consistent with a Cepheid, although the spectral type derived from our own work was a K1.5 III.

The primary calibrator HD 165459 was found to have a significant excess (∼40%) at 24 μm in the MIPS (Multiband Imaging Photometer for *Spitzer*) calibration program. Presumably, this excess is due to a disk around the star, such as in other "Vega"-type A stars. Is there any evidence for this disk at IRAC wavelengths? Calibrating the measured fluxes with the new calibration factors, we find that the star's flux relative to the photospheric model is 0.982 ± 0.020, 0.987 ± 0.024, 0.976 ± 0.022, and 0.993 ± 0.022 in channels 1, 2, 3, and 4, respectively. Since these are absolute measurements, we have used σ_{rms} from Table 7 as the calibration uncertainty (combined with the uncertainty in this individual star's measurements). In fact, we can remove the absolute uncertainty in the size of the star by normalizing all fluxes at 3.6 μm. Then the ratio of observed to photospheric flux, assuming there is no excess at 3.6 μm, is 1.006 ± 0.009, 0.994 ± 0.009, and 1.011 ± 0.008 in channels 2, 3, and 4, respectively. It appears that there is no mid-infrared excess for this star in the 3.6–8 μm range, at a 95% confidence upper limit of 4% (with no assumptions), or at 4.5, 5.8, or 8 μm, at a 95% confidence limit of 1.2%, 1.8%, or 1.6% (assuming no excess at 3.6 μm).

7. CONCLUSIONS

The Infrared Array Camera on the *Spitzer Space Telescope* has a stable gain on all measured timescales, making it possible to measure variability at the 2% level for carefully reduced data. The absolute calibration using stellar photospheric models scaled to ground-based photometry at optical through near-infrared wavelengths is accurate to 1.8%, 1.9%, 2.0%, and 2.1% in channels 1 (3.6 μm), 2 (4.5 μm), 3 (5.8 μm), and 4 (8 μm), respectively. To measure fluxes at this high level of accuracy requires several photometric corrections: array position dependence (due to changing spectral response and pixel solid angle over the camera field of view), pixel phase dependence (due to nonuniform quantum efficiency over a pixel), color correction (due to the different system response integrated over the passband for sources of different color), and aperture correction (due to the fractions of light included within the measurement aperture and lost in the background aperture).

REFERENCES

Beichman, C. A., Neugebauer, G., Habing, H. J., Clegg, P. E., & Chester, T. J. 1988, *Infrared Astronomical Satellite* (*IRAS*) Catalogs and Atlas, Vol. 1, Explanatory Supplement (NASA RP-1190; Washington: NASA)

Blommaert, J., et al. 2003, CAM—The *ISO* Camera, *ISO* Handbook, Vol. 2, Ver 2.0 (Noordwijk: ESA), (http://www.iso.vilspa.esa.es/manuals/HANDBOOK/cam_hb)

Cohen, M. 2003, in Proc. The Calibration Legacy of the *ISO* Mission, ed. L. Metcalfe et al. (ESA SP-481; Noordwijk: ESA), 135

Cohen, M., Megeath, S. T., Hammersley, P. L., Martín-Luis, F., & Stauffer, J. 2003, AJ, 125, 2645

Cohen, M., Walker, R. G., Carter, B., Hammersley, P., Kidger, M., & Noguchi, K. 1999, AJ, 117, 1864

Cohen, M., Witteborn, F. C., Carbon, D. F., Davies, J. K., Wooden, D. H., & Bregman, J. D. 1996, AJ, 112, 2274

Drilling, J. S., & Landolt, A. U. 1979, AJ, 84, 783

Fazio, G. G., et al. 2004, ApJS, 154, 10

Hauser, M. G., et al. 1998, COBE Diffuse Infrared Background Experiment (DIRBE) Explanatory Supplement (Washington: GSFC), (http://lambda.gsfc.nasa.gov/product/cobe/dirbe_exsup.cfm)

Klemola, A. R., Jones, B. F., & Hanson, R. B. 1987, AJ, 94, 501

Kümmel, M. W., & Wagner, S. J. 2000, A&A, 353, 867

Kurucz, R. L. 1993a, Kurucz CD-ROM 18, SYNTHE Spectrum Synthesis Programs and Line Data (Cambridge: SAO)

———. 1993b, CD-ROM 13, ATLAS9 Stellar Atmosphere Programs and 2 km/s Grid (Cambridge: SAO)

Megeath, S. T., Cohen, M., Stauffer, J., Hora, J., Fazio G., Berlind, P., & Calkins, M. 2003, in Proc. The Calibration Legacy of the *ISO* Mission, ed. L. Metcalfe et al. (ESA SP-481; Noordwijk: ESA), 165

Pojmański, G. 2000, Acta Astron., 50, 177

Price, S. D., Paxson, C., Engelke, C., & Murdock, T. L. 2004, AJ, 128, 889

Skrutskie, M. F. 1999, in Astrophysics with Infrared Surveys: A Prelude to *SIRTF*, ed. M. D. Bicay et al. (San Francisco: ASP), 185

Werner, M. W., et al. 2004, ApJS, 154, 1